

Moiré physics in two-dimensional materials: Novel quantum phases and electronic properties

Zi-Yi Tian(田子弈), Si-Yu Li(李思宇), Hai-Tao Zhou(周海涛), Yu-Hang Jiang(姜宇航), and Jin-Hai Mao(毛金海)

Citation: Chin. Phys. B, 2025, 34 (**2**): 027301. DOI: 10.1088/1674-1056/ad9e96
Journal homepage: http://cpb.iphy.ac.cn; http://iopscience.iop.org/cpb

What follows is a list of articles you may be interested in

Peak structure in the interlayer conductance of Moiré superlattices

Yizhou Tao(陶懿洲), Chao Liu(刘超), Mingwen Xiao(肖明文), and Henan Fang(方贺男)
Chin. Phys. B, 2024, 33 (**10**): 107301. DOI: 10.1088/1674-1056/ad655b

Lower bound on the spread of valley splitting in Si/SiGe quantum wells induced by atomic rearrangement at the interface

Gang Wang(王刚), Shan Guan(管闪), Zhi-Gang Song(宋志刚), and Jun-Wei Luo(骆军委)
Chin. Phys. B, 2023, 32 (**10**): 107309. DOI: 10.1088/1674-1056/acf208

Moiré Dirac fermions in transition metal dichalcogenides heterobilayers

Chenglong Che(车成龙), Yawei Lv(吕亚威), and Qingjun Tong(童庆军)
Chin. Phys. B, 2023, 32 (**10**): 107307. DOI: 10.1088/1674-1056/aceee5

Epitaxial growth of trilayer graphene moiré superlattice

Yalong Yuan(袁亚龙), Yanbang Chu(褚衍邦), Cheng Hu(胡成), Jinpeng Tian(田金朋), Le Liu(刘乐), Fanfan Wu(吴帆帆), Yiru Ji(季怡汝), Jiaojiao Zhao(赵交交), Zhiheng Huang(黄智恒), Xiaozhou Zan(昝晓洲), Luojun Du(杜罗军), Kenji Watanabe, Takashi Taniguchi, Dongxia Shi(时东霞), Zhiwen Shi(史志文), Wei Yang(杨威), and Guangyu Zhang(张广宇)
Chin. Phys. B, 2023, 32 (**7**): 077304. DOI: 10.1088/1674-1056/accdc8

Emerging properties of two-dimensional twisted bilayer materials

Yang Cheng(程阳), Chen Huang(黄琛), Hao Hong(洪浩), Zixun Zhao(赵子荀), Kaihui Liu(刘开辉)
Chin. Phys. B, 2019, 28 (**10**): 107304. DOI: 10.1088/1674-1056/ab3e46

TOPICAL REVIEW — Moiré physics in two-dimensional materials

Moiré physics in two-dimensional materials: Novel quantum phases and electronic properties

Zi-Yi Tian(田子弈)[1], Si-Yu Li(李思宇)[2], Hai-Tao Zhou(周海涛)[3,†], Yu-Hang Jiang(姜宇航)[1,‡], and Jin-Hai Mao(毛金海)[4,§]

[1] *College of Materials Science and Opto-Electronic Technology, Center of Materials Science and Optoelectronics Engineering, University of Chinese Academy of Sciences, Beijing* 100049, *China*

[2] *Institute of Physics, Chinese Academy of Sciences, Beijing* 100049, *China*

[3] *Beijing Institute of Aeronautical Materials, Aero Engine Corporation of China, Beijing* 100095, *China*

[4] *School of Physical Sciences, University of Chinese Academy of Sciences, Beijing* 100049, *China*

(Received 9 September 2024; revised manuscript received 4 December 2024; accepted manuscript online 13 December 2024)

Moiré superlattices have revolutionized the study of two-dimensional materials, enabling unprecedented control over their electronic, magnetic, optical, and mechanical properties. This review provides a comprehensive analysis of the latest advancements in moiré physics, focusing on the formation of moiré superlattices due to rotational misalignment or lattice mismatch in two-dimensional materials. These superlattices induce flat band structures and strong correlation effects, leading to the emergence of exotic quantum phases, such as unconventional superconductivity, correlated insulating states, and fractional quantum anomalous Hall effects. The review also explores the underlying mechanisms of these phenomena and discusses the potential technological applications of moiré physics, offering insights into future research directions in this rapidly evolving field.

Keywords: two-dimensional quantum material, moiré superlattice, flat band, strong correlations

PACS: 73.21.Cd, 73.22.–f, 73.21.–b, 71.27.+a

DOI: 10.1088/1674-1056/ad9e96 **CSTR:** 32038.14.CPB.ad9e96

1. Introduction

The advent of two-dimensional materials (2DMs), such as graphene and hexagonal boron nitride (hBN), has profoundly impacted condensed matter physics and materials science, particularly in the 21st century. These materials, defined by their atomic-scale thickness, exhibit a wide range of electronic properties, spanning superconductors (e.g., $NbSe_2$), metals, semiconductors with tunable bandgaps (e.g., black phosphorus, MoS_2, WSe_2), and insulators (e.g., hBN). The unique combination of diverse intrinsic properties and the ability to tune these characteristics through experimental approaches such as electrostatic gating and substrate engineering have positioned 2DMs as a versatile platform for exploring emergent quantum phenomena and enabling new functionalities in electronic and quantum technologies.

Moiré heterostructures are constructed by either the rotational misalignment of identical 2DMs or the lattice mismatch of different 2DMs, in which moiré superlattices arise from inference between the two constituent atomic crystals. The enlarged moiré superlattices cause a folding mini-Brillouin zone (BZ) smaller than the original one, when combined with band repulsion, new band gaps can be opened. Due to these effects, band flattening takes place, further quenching the kinetic energy of electrons and resulting in the dominant roles of Coulomb interaction energies in the systems. In addition, so-obtained flat electronic bands are generically topological and exhibit non-zero Berry curvature. These characteristics contribute to producing exotic quantum phases in moiré heterostructures, such as correlation-driven topological phases. Some of these characteristics are even without single-particle analogues, such as fractional Chern insulators (FCIs).

In this review, we systematically introduce the recent progresses of moiré physics in 2DMs. We summarize experimental observations of novel quantum states in moiré heterostructures, such as unconventional superconductivity, correlated insulating states, and quantum anomalous Hall effects (QAHEs), and briefly discuss their underlying mechanisms. Furthermore, we offer our perspectives on the future exploration of moiré physics and its potential technological applications.

2. Formation of moiré superlattices

When two two-dimensional (2D) van der Waals (vdW) layered materials with similar lattice constants are stacked at some special twist angles, the difference in lattice parameters

†Corresponding author. E-mail: 13811517657@139.com

‡Corresponding author. E-mail: yuhangjiang@ucas.ac.cn

§Corresponding author. E-mail: jhmao@ucas.ac.cn

© 2025 Chinese Physical Society and IOP Publishing Ltd. All rights, including for text and data mining, AI training, and similar technologies, are reserved.

and the angle of interlayer rotation give rise to a new moiré superlattice structure. Among the most prominent examples are the graphene/h-BN heterostructure moiré superlattices gained attention in 2013,[1–5] and the "magic-angle" graphene discovered in 2018.[6,7] The former serves as a model for single-particle energy band modulation via two-dimensional superlattices, while the latter has garnered significant attention due to its flat-band structure, which leads to the emergence of correlated insulating states and superconductivity. This discovery has positioned magic-angle twisted bilayer graphene as a novel strongly correlated system within condensed matter physics.

For the twisted bilayer graphene (TBG), Schmidt *et al.*[8] demonstrated that rotating bilayer graphene at any twist angle can be artificially achieved experimentally. But periodic moiré patterns emerge only when the superlattice exhibits a commensurate structure, which occurs only at specific twist angles. A superlattice with a commensurate structure possesses both translational and rotational symmetries, whereas a superlattice with an incommensurate structure retains only rotational symmetry. Such a superlattice with a commensurate structure and moiré patterns is called the moiré superlattice. Structurally speaking, this superlattice comes from the mismatch of lattice structures. When the lattice constants between the stacked lattices are different or there is a relative twist angle, lattice mismatch occurs, and then a superlattice structure is produced. There are two types of moiré superlattices: homojunction and heterojunction moiré superlattices. The two cases are discussed respectively. In the homojunction, since the materials have the same lattice constant, the formation of a superlattice can only be achieved by adjusting the interlayer twist angle. Now consider the TBG as the example of the homojunction.

In the primitive cell of monolayer graphene, there exist two inequivalent carbon atoms (A and B). And there are two common ways of stacking for bilayer graphene: turbostratic stacking (AA) and Bernal stacking (AB). Turbostratic stacking means the A atoms and B atoms corresponding to the top and bottom layers are coincident respectively, while Bernal stacking means the A atoms of the top layer are coincident with the B atoms of the bottom layer.

The twist angle is defined as the angle between the top and bottom lattice vectors. Take the basis vectors in the primitive cell of the monolayer graphene as $\boldsymbol{a}_1 = a_0(\frac{3}{2}, -\frac{\sqrt{3}}{2})$ and $\boldsymbol{a}_2 = a_0(\frac{3}{2}, -\frac{\sqrt{3}}{2})$. a_0 is the lattice constant of the primitive cell, $a_0 = 0.246$ nm. Then the twist angle θ is given by

$$\cos\theta = \frac{3i^2+3i+\frac{1}{2}}{3i^2+3i+1}, \quad i = 0,1,2,\ldots. \tag{1}$$

So the period of the superlattice is $L = \sqrt{3i^2+3i+1}a_0$. When $i = 0$, the TBG turns to the turbostratic stacking (AA) bilayer graphene. And when $i \to \infty$, the TBG turns to the Bernal stacking (AB) bilayer graphene.

The basis vectors of the new primitive cell of the moiré superlattice are

$$\boldsymbol{T}_1 = i\boldsymbol{a}_1 + (i+1)\boldsymbol{a}_2, \tag{2}$$

$$\boldsymbol{T}_2 = -(i+1)\boldsymbol{a}_1 + (2i+1)\boldsymbol{a}_2. \tag{3}$$

The reciprocal lattice vectors are

$$\boldsymbol{G}_1 = \frac{4\pi}{3(3i^2+3i+1)}[(3i+1)\boldsymbol{a}_1 + \boldsymbol{a}_2], \tag{4}$$

$$\boldsymbol{G}_2 = \frac{4\pi}{3(3i^2+3i+1)}[-(3i+2)\boldsymbol{a}_1 + (3i+1)\boldsymbol{a}_2]. \tag{5}$$

The length of the side of the first Brillouin zone is given by[11]

$$|\Delta\boldsymbol{K}| = |\boldsymbol{K}_1 - \boldsymbol{K}_2| = 2|\boldsymbol{K}|\sin\left(\frac{\theta}{2}\right) = \frac{1}{\sqrt{3}}|\boldsymbol{G}|, \tag{6}$$

where $|\boldsymbol{K}|$ is the length of the side of the first Brillouin zone of monolayer graphene, and $\Delta\boldsymbol{K}$ is the relative position vector of the Dirac points of the top and bottom monolayer graphene. The lattice and the reciprocal lattice of the TBG are shown in Fig. 1.

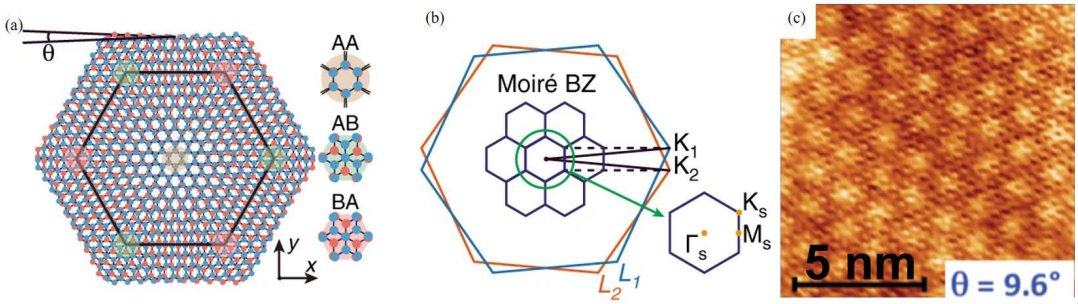


Fig. 1. Moiré pattern of TBG.[9,10] (a) Schematic of general twisted bilayer systems with the twist angle $\theta = 4.4°$, where the largest black hexagon denotes moiré superlattices including AA and AB/BA stacked lattices. Blue (red) dots represent the sites in L1 (L2). (b) Schematic of BZs. Sky blue and red hexagons represent first BZs for L1 and L2 while black hexagons represent moiré BZs (mBZ). (c) Scanning tunneling microscope (STM) images of TBG with $\theta = 9.5°$. The scale bar is 5.0 nm.

In the heterojunction, for the not equal lattice constants of two materials, the formation of a superlattice can be achieved without adjusting the interlayer twist angle. At the same time, the moiré superlattice can be modulated by adjusting the twist angle.

Consider the hBN (hexagonal boron nitride)/graphene heterojunction as the example of the heterojunction. If we take both the lattice mismatch ($\delta = 1.8\%$ for graphene and hBN[12]) and the twist angle (θ) into consideration, the period of the moiré superlattice L is given by[4]

$$L = \frac{(1+\delta)a_0}{\sqrt{2(1+\delta)(1-\cos\theta)+\delta^2}}. \tag{7}$$

It can be concluded that when the twist angle is zero ($\theta = 0°$), the moiré superlattice has a maximum period of about 13.8 nm.

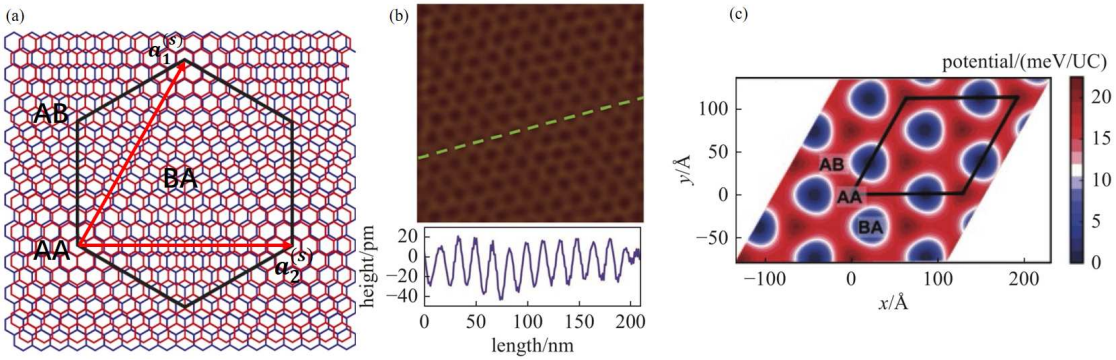


Fig. 2. Superlattice of hBN/graphene heterojunction.[11,13] (a) Schematic diagram of graphene/hBN superlattice formed with twist angle of 0°, with hBN represented in blue, and graphene in red. Black hexagons mark the moiré plaquette and red arrows mark the basis vectors, with carbon atoms in gray. Different stacking regions are present within the superlattice. (b) The upper part shows the morphology image of graphene/boron nitride characterized by AFM, while the lower part represents the height variations along the green line. (c) Spatial distribution of the interlayer interaction potential in the graphene/boron nitride superlattice with twist angle of 0°.

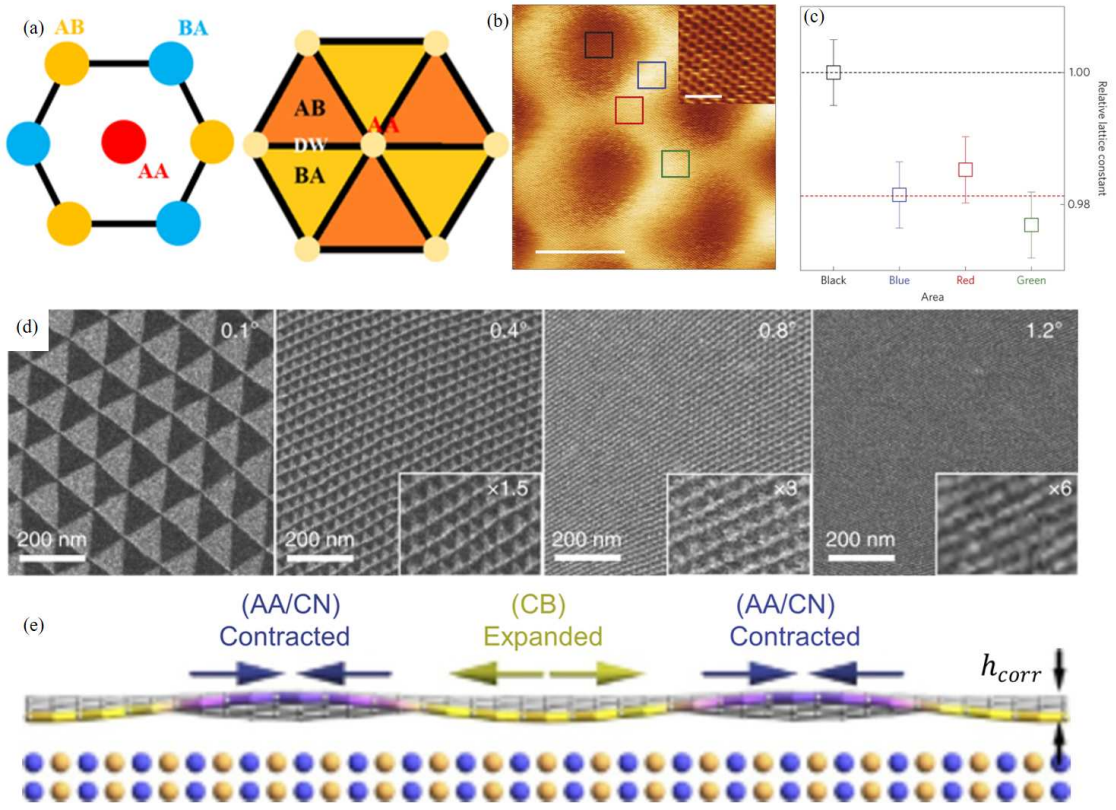


Fig. 3. Atomic reconstruction of moiré superlattice.[13–16] (a) Schematic diagram depicting the stacking types of unreconstructed twisted bilayer graphene (left) and reconstructed twisted bilayer graphene (right). (b) STM images of the graphene/hBN heterojunction sample with twist angle of 0° and their local magnifications (as shown in the upper-right inset), with a scale bar of 10 nm. The size of the square region is 3 nm × 3 nm. Inset: A magnified view of the black square region, showing clear atomic structures with a scale bar of 1 nm. (c) Relative lattice constants of different color regions within the images in panel (b), corresponding to the colors in panel (b). (d) Dark-field transmission electron microscope images obtained by selecting graphene diffraction peaks in TBG, with twist angles of 0.1°, 0.4°, 0.8°, and 1.2°, respectively. (e) Due to the spatially modulated vdW adhesion potential, the graphene lattice periodically expands and contracts in-plane. An out-of-plane corrugation profile also develops, both matching the moiré.

3. Atomic reconstruction

When two monolayer materials form a two-dimensional moiré superlattice structure, the lattices of one or both monolayers may become distorted due to the spatially modulated vdW adhesion potential. Furthermore, the surfaces of the materials are typically not perfectly flat. This phenomenon is referred to as atomic reconstruction.

According to the recent work,[14,15] atomic reconstruction is particularly pronounced when the twist angle of the twisted bilayer graphene is near 0°, resulting in discrete symmetric domains. The energy of AA stacking is the highest, followed by BA stacking, and AB stacking has the lowest energy. To minimize the overall energy, atomic reconstruction occurs on the surface. The regions of AB and BA stacking expand to form triangular areas, separated by domain walls. The intersections of these domain walls correspond to AA stacking sites, ultimately leading to a periodic structure where AB and BA stackings alternate. Each AB stacking domain is surrounded by three adjacent BA stacking domains (and vice versa), as shown in Fig. 2. Moreover, Yoo *et al.* found that when the twist angle increased, the region of atomic reconstruction gradually decreased, and the contrast significantly weakened, and finally became close to unidirectional fringes (as shown in Fig. 3(d)). This trend indicates that both the reconstruction intensity and the contrast in the domain increase with the decrease of the twist angle. This effect is also seen in heterojunctions composed of transition metal dichalcogenides (TMDs), such as $MoSe_2/WSe_2$.[17]

For the graphene/hBN heterojunction structure, graphene overlaid on hexagonal boron nitride also undergoes minor stress adjustments in response to the periodicity of the hBN, thereby resulting in atomic reconstruction,[13,14] as shown in Fig. 3(e). Moreover, experiments have demonstrated that atomic reconstruction significantly affects the atomic structure of domain walls.[13,18,19] Woods *et al.*[13] found that the relative lattice constants in the domain wall regions of monolayer graphene/hexagonal boron nitride are smaller than those in the uniform regions (as shown in Figs. 3(b) and 3(c)), suggesting that the lattice within the domain wall areas is likely compressed, thereby providing strong evidence for the occurrence of atomic reconstruction.

4. Modulation of the band structure by moiré superlattices

4.1. Van Hove singularities

The Van Hove singularity is a phenomenon resulting from the band modulation of a superlattice structure, which refers to points in the electronic structure where the state density diverges.[20] Saddle points, as well as local maxima or minima in the electronic band structure, can all potentially become Van Hove singularities. In twisted systems, Van Hove singularities typically originate from saddle points in the band structure.

This phenomenon was discovered in epitaxially grown twisted bilayer graphene (TBG) even before the observation in graphene/hexagonal boron nitride superlattices. Figure 4(a) illustrates the formation of a Van Hove singularity in TBG. When the two layers of graphene are relatively rotated, their Brillouin zones also rotate, causing a separation of the Dirac cones in reciprocal space.[21,22] The offset between the two Dirac cones can be calculated using Eq. (6).[11] The separation inevitably leads to the formation of a saddle point at the intersection of the two Dirac cones. In the band structure, this point is a local maximum along the direction of cone separation and a local minimum in the energy axis (vertical direction). Theoretically, Van Hove singularities tend to appear in pairs and are related to the twist angle and the interlayer coupling strength. The energy difference between a pair of Van Hove singularities $\Delta E_{\rm vhs}$ can be roughly estimated using[27]

$$\Delta E_{\rm vhs} \approx \hbar v_{\rm F} \Delta K - 2t_\theta, \tag{8}$$

where $v_{\rm F}$ denotes the renormalized Fermi velocity, and t_θ denotes the interlayer coupling coefficient.

A multitude of studies have demonstrated that the location and energy difference of the Van Hove singularities $E_{\rm vhs}$ can be approximately divided into three intervals with respect to the relative twist angle θ. When the angle is greater than 10°, the saddle point energy is significantly separated from the Dirac point, leading to a tendency for interlayer electrons to decouple. The low-energy band structure appears as a mere superposition of the Dirac cones of single-layer graphene.[27–30] In the range of 2° to 10°, the value of $E_{\rm vhs}$ decreases with the diminishing angle θ,[10,28] yet the energy symmetry center of the two Van Hove singularities remains nearly invariant with the angle,[24] as illustrated in Fig. 4(c). Below 2°, the Van Hove singularities exhibit spatial localization,[10,23,25,31] and the density of states begins to cluster around the AA stacking regions,[10] as evident from Fig. 4(d). Consequently, as the Fermi energy further approaches the energy of the Van Hove singularities, a strongly localized charge density wave is observed.[23]

Scanning tunneling microscopy (STM) is the preferred tool for studying Van Hove singularities because it not only allows for the deduction of the twist angle of twisted bilayer graphene (TBG) through the moiré patterns observed in the topography images, but also enables the measurement of the local electronic state density at a given spatial point. Additionally, STM can determine the Landau level spectrum under a magnetic field, which provides information about the Fermi velocity of electrons and the strength of interlayer coupling.

The Landau level spectrum for massless Dirac fermions under a certain magnetic field satisfies the following

relationship:[25]

$$E_n = E_{\rm D} + {\rm sgn}(n)\sqrt{2e\hbar v_{\rm F}^2\,|n|B}, \tag{9}$$

where $E_{\rm D}$ denotes the energy of the Dirac point, $v_{\rm F}$ denotes the Fermi velocity, and B denotes the magnitude of the external magnetic field. By measuring the dependency relationship between a series of energy levels and $(|n|B)^{\frac{1}{2}}$, one can determine the magnitude of the Fermi velocity from the slope. When the angle θ is slightly greater than 3°, the strength of the interlayer coupling (t_θ) can also be obtained through the formula for the renormalized Fermi velocity:[11]

$$\frac{v_{\rm F}(\theta)}{v_{\rm F}^0} = 1 - 9\left(\frac{t_\theta}{\hbar v_{\rm F}^0 \Delta K}\right)^2. \tag{10}$$

The Fermi velocity calculated using this formula is consistent with experimental results (as shown in Fig. 4(e)). It is evident that whether the magnitude of the renormalized Fermi velocity depends on the angle θ is influenced by the strength of the interlayer coupling.[27] When the interlayer coupling is sufficiently weak, the Fermi velocity becomes independent of the angle θ.[26,31]

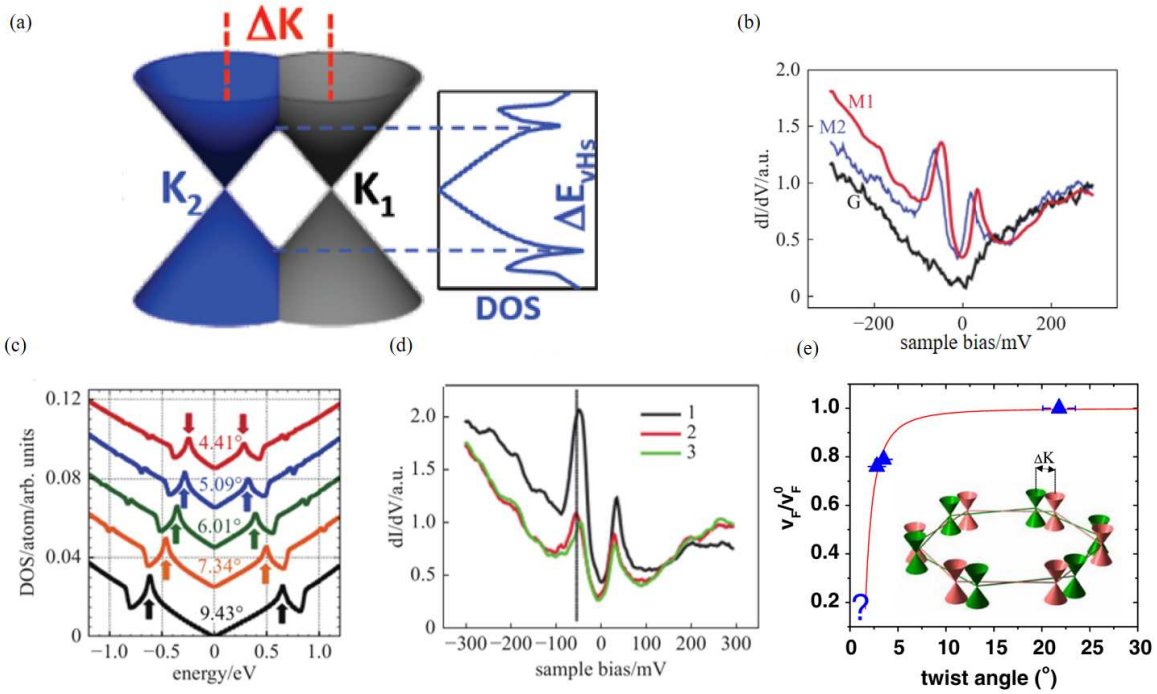


Fig. 4. Van Hove singularities.[10,21–26] (a) Schematic diagram illustrating the formation of Van Hove singularities (VHS). VHS forms between the two Dirac cones, resulting in a higher electron density at the singularity point. (b) Scanning tunneling spectroscopy (STS) curves for graphene. G represents the STS curve for a single layer graphene, while M1 and M2 represent STS curves for twisted bilayer graphene with $\theta = 1.79°$, where VHS is clearly observed on both sides of the Dirac point. (c) When the angle is between 2° and 10°, the $E_{\rm vhs}$ value decreases as the angle θ decreases, but the energy center of the two VHS points remains almost unchanged with varying angles. (d) STS spectra of twisted bilayer graphene with $\theta = 1.79°$, where 1 corresponds to the AA-stacked region, and 2 and 3 correspond to other stacking regions. While all spectra display two peaks, the electron density at position 1 is significantly higher than that at other positions. (e) Relationship between the reorganized Fermi velocity and the interlayer twist angle. The red curve represents the fitted curve obtained from formula (10), while the blue triangles correspond to experimentally measured data. The localization phenomenon at the AA-stacked position occurs around a twist angle of approximately 1.16° as mentioned in the text.

In addition to the conclusions mentioned earlier, there is extensive research on the physical properties of Van Hove singularities. For instance, by adjusting the position of the Fermi level in TBG through electrostatic doping, the system can exhibit many-body quantum phenomena when the Fermi level is close to the energy of the Van Hove singularity.[32] In the field of optics, when the energy of the excited photons matches the energy difference $\Delta E_{\rm vhs}$ of the Van Hove singularity, the amplitude of the G-mode phonons in the Raman spectrum is significantly enhanced.[33] Moreover, higher-order Van Hove singularities can be induced in TBG by applying pressure, or in trilayer graphene by applying a perpendicular electric field.[34]

4.2. Secondary Dirac points

Secondary Dirac points (SDPs) are a typical phenomenon in which the moiré superlattice potential changes the band structure of graphene. It is theorized that under the modulation of moiré lattice potential, there will be a dispersion relationship similar to the graphene Dirac points at the boundary of the Brillouin region, which is called secondary Dirac point.[35–38] Experimental observation of SDP can be achieved on graphene/hexagonal boron nitride superlattices. SDPs can be observed using STM. The presence of SDPs is verified by observing whether there are local minima on both sides of the primary Dirac point (the minimum in the spectral line) in the

scanning tunneling spectrum.[4] Additionally, STM measurements have found that a corrugated graphene monolayer on Rh foil can provide a weak periodic potential, thereby inducing SDPs.[41]

Angle-resolved photoelectron spectroscopy (ARPES) is one of the prevalent methods employed in the study of SDP. Due to its exceptionally high momentum and energy resolution, ARPES can accurately pinpoint the location of SDPs in momentum space and determine the magnitude of the energy gap. This measurement technique requires samples of graphene/hexagonal boron nitride of exceptional quality, with the size of the uniform periodic regions to be at least 50 μm. Traditional mechanical exfoliation transfer methods often fall short in meeting these size requirements for samples. However, this challenge has been overcome by the advanced epitaxial growth techniques. Figures 5(c) and 5(d) showcase the use of ARPES on epitaxially grown graphene/hexagonal boron nitride samples, revealing an energy gap of approximately 100 meV associated with SDPs. This observation confirms that the disruption of inversion symmetry leads to the formation of an energy gap at the primary Dirac point as well as the SDPs.[40]

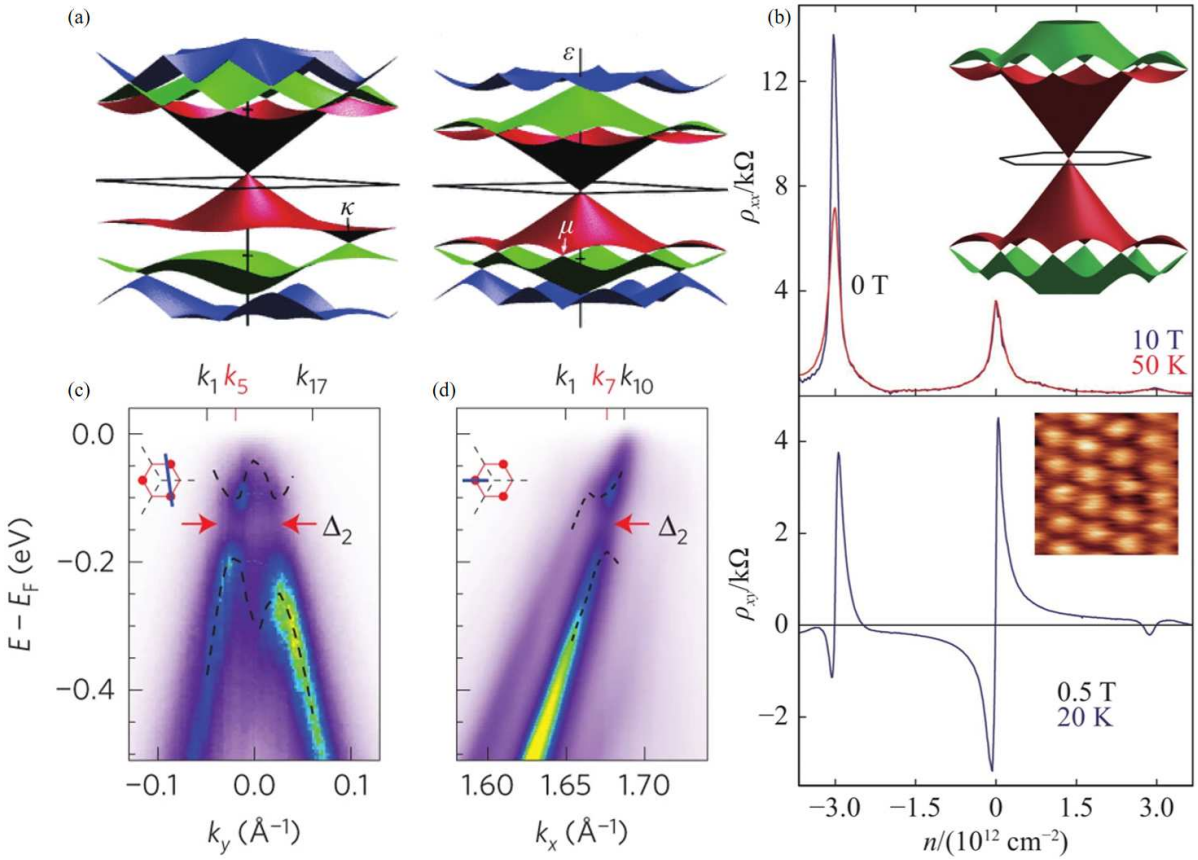


Fig. 5. Secondary Dirac points.[3,39,40] (a) The electronic band structure of graphene near the κ point on boron nitride with a small misalignment angle, $\theta \ll 1$. In the left image, there is an isolated saddle point (SDP) in the valence band at the κ point. In the right image, there is an SDP at the μ point. (b) Transport properties of Dirac fermions in moiré superlattices of hBN/graphene heterojunction, $\theta = 0 \pm 1°$. Upper image: Longitudinal resistivity as a function of carrier concentration, exhibiting a peak in resistivity at the SDP with a strong temperature dependency. Lower image: Hall resistivity as a function of carrier concentration, showing a change in sign of the Hall resistivity at the SDP. (c) and (d) ARPES observations of gapped main Dirac point (c) and SDP (d), for 0° aligned graphene/hBN.

4.3. Flat bands

Flat bands can arise from electron motion on specific lattices with particular geometric arrangements, hopping parameters, and filling factors, often exhibiting unique topological properties under certain conditions, such as specific electron filling and interaction strengths. Their reduced bandwidth proportionally enhances the effect of Coulomb interaction, even when the absolute magnitude of the latter is relatively small.[42] Therefore, systems with flat bands often exhibit strong correlation effects. In moiré materials, the presence of interlayer electron transition, combined with band repulsion, jointly produces flat bands under suitable conditions.

In TBG, the Fermi velocity of electrons is dependent on the interlayer coupling strength and the twist angle between the layers.[43] At large angles, the interlayer coupling strength can be treated using perturbation theory; however, at small angles, the interlayer coupling strength can no longer be considered a perturbation, and the electronic properties become increasingly complex. Based on these factors, MacDonald and Bistritzer constructed a continuum model Hamiltonian com-

posed of two single-layer Hamiltonians and a tunneling term related to interlayer coupling. This model predicted the disappearance of the electron Fermi velocity at a set of discrete angles (see Fig. 6(c)), which corresponds to the emergence of flat bands. Furthermore, researchers have predicted that at small angles, the relative translation between layers almost does not alter the electronic properties.[43] However, due to the influence of the relative atomic positions between layers on interlayer electron tunneling, differences exist between electrons in different moiré regions. The theory indicates that the electron wave function tends to localize in regions of approximate AA stacking,[30] and these properties have been confirmed in subsequent experiments.[45–47]

Although electron–electron interactions are not considered in the continuum model, the Fermi velocity of electrons in flat bands approaches zero, and they localize within the superlattice. Consequently, the interaction energy between electrons, $V_C = \frac{e^2}{4\pi\epsilon d}$ (where d is the effective distance between electrons, on the same scale as the moiré lattice period), significantly exceeds their kinetic energy. This becomes the dominant factor affecting the physical properties of the region, leading to a substantial alteration. Numerous subsequent experiments have confirmed the impact of these strong electron–electron correlations. For instance, in STS spectra, the presence of flat bands increases the density of localized electronic states near zero energy. Therefore, when flat bands are either completely filled or unfilled, the STS spectra exhibit a sharp peak, corresponding to single-particle behavior. However, when flat bands are partially filled, the corresponding peak in the STS spectra broadens, and a noticeable band splitting occurs.[46,48,49] This is due to the symmetry breaking caused by strong electron–electron interactions, which splits the degenerate flat bands into sub-bands, indicative of many-body behavior induced by strong correlations.

Similar to the magic angle graphene systems, the presence of the moiré periodic potential in TMD moiré superlattices can result in the emergence of flat bands, potentially enabling a range of correlated and topological electronic states. Theoretically, MacDonald's research group[44] first proposed in 2018 that in TMD moiré superlattice heterojunctions, the physics of the flat bands can be described using a single-band Hubbard model on a triangular lattice, see Fig. 6(d). This is because the Wannier orbitals are predominantly localized at specific high-symmetry stacking points of the moiré superlattice. Moreover, the model parameters can be tuned by varying parameters such as the twist angle, thus making it possible in principle to use these systems as a new type of quantum simulator for the Hubbard model. When the flat moiré bands are partially filled, candidate many-body ground states at some special filling factors include spin-liquid states, quantum anomalous Hall insulators and chiral d-wave superconductors.

In the following sections, novel physical phenomena related to strong correlations between electrons induced by flat bands will be introduced.

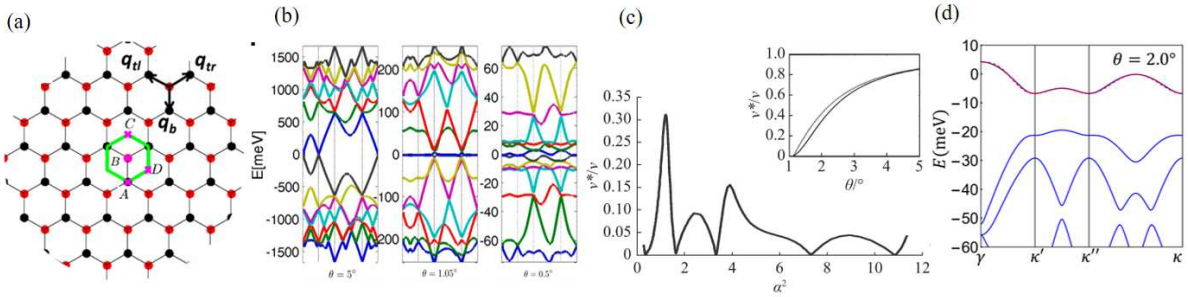


Fig. 6. Flat bands.[43,44] (a) The three equivalent Dirac points in the first Brillouin zone result in three distinct hopping processes. Interference between hopping processes with different wave vectors captures the spatial variation of interlayer coordination that defines the moiré pattern. (b) Energy dispersion for the 14 bands closest to the Dirac point plotted along the k-space trajectory $A \to B \to C \to D \to A$ for $w = 110$ meV, and $\theta = 5°$ (left), 1.05° (middle), and 0.5° (right). (c) At certain angles corresponding to α, the reorganized Fermi velocity becomes zero, leading to flat bands. $\alpha = w/(vk_\theta)$; w is the hopping energy; $k_\theta = 2k_D \sin(\theta/2)$, where k_D is the magnitude of the Brillouin-zone corner wave vector for a single layer; v is the Dirac velocity. (d) Moiré bands of WSe_2 on $MoSe_2$ at twist angle $\theta = 2.0°$. The red dashed line is a tight-binding-model fit to the highest valence band that includes hopping up to the third nearest neighbor and has a narrow bandwidth (about 11 meV).

5. Correlated electronic states and topological electronic states

5.1. Correlated insulating states and superconducting states

Since the successful fabrication of magic-angle graphene, the correlated insulating states and superconductivity observed in these materials have garnered significant attention. This phenomenon was first observed in twisted bilayer graphene (TBG), where Cao *et al.* utilized an improved "tear and stack" method to prepare TBG near the magic angle (1.1°) in 2018.[7] By fabricating the sample into a field-effect transistor structure and adjusting the gate voltage to control the carrier concentration, they investigated the electronic properties at various flat band fillings. Due to the eightfold degeneracy associated with

spin and valley degrees of freedom in TBG's flat band, full filling corresponds to an average of 8 electrons per moiré unit cell, with an electron density required to fill one flat band being $n_s \approx 2.7 \times 10^{12}$ cm^{-2}. When the flat band is fully occupied by electrons or holes (i.e., carrier concentration $n = \pm n_s$), the system exhibits insulating behavior with zero conductance, as confirmed by Cao *et al.*'s measurements. However, at half-filling of the flat band ($n = \pm n_s/2$, filling factor $\nu = \pm 2$), an insulating state was observed instead of the expected metallic state (as shown in Fig. 7(a)). This occurs because, near the magic angle, the electrons' kinetic energy becomes negligible compared to their Coulomb interaction energy, causing the fourfold degenerate flat band to split into two, leading to a Mott-like insulating state.[50] Furthermore, due to orbital and Zeeman effects, the split bands exhibit spin-singlet states in response to magnetic fields applied in different directions.

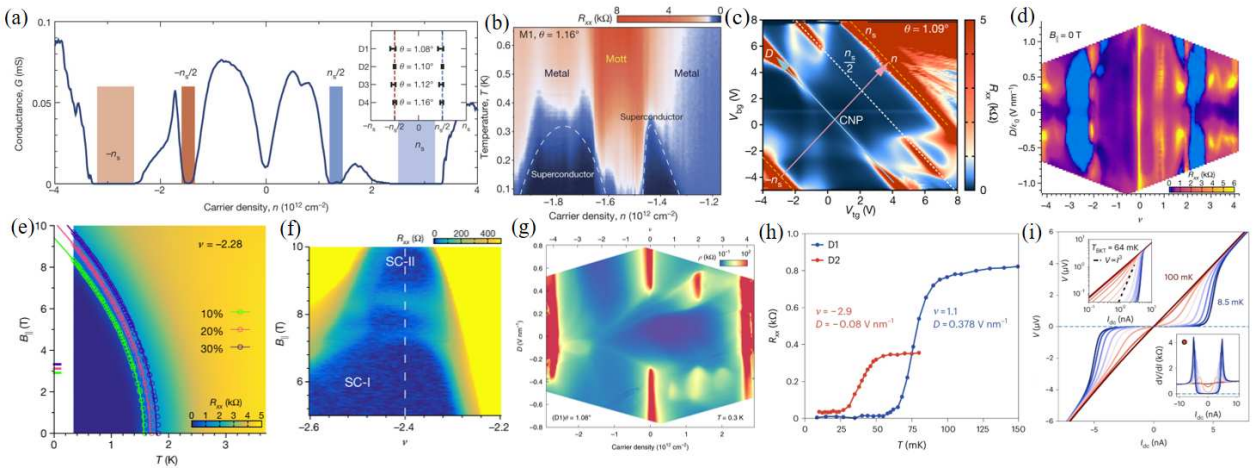


Fig. 7. Correlated insulating states and superconducting states.[6,7,51–55] (a) The conductivity in TBG with $\theta = 1.08°$ and $T = 0.3$ K as a function of carrier concentration, exhibiting an insulating state at half-filling $\nu = \pm 2$. (b) Phase diagram near $\nu = -2$ in TBG with $\theta = 1.16°$, showing superconducting phases slightly away from half-filling on both sides of the carrier concentration. (c) Adjustment of the electric displacement field and carrier concentration in TDBG with $\theta = 1.09°$ by tuning the top and bottom gate voltages. Under electric field tuning, the emergence of correlated insulating states is observed at the electron half-filling. (d) Phase diagram of high-quality MATTG devices, concerning carrier concentration and electric displacement field, with the presence of superconducting states near integer fillings. (e) Longitudinal resistivity in MATTG at $\nu = -2.28$ as a function of temperature and parallel magnetic field, showing that TTG's superconductivity is not limited by the Pauli limit and can exist under magnetic fields as high as 10 T. (f) Longitudinal resistivity in MATTG as a function of filling and parallel magnetic field. As the magnetic field increases, the appearance of a second superconducting phase can be observed, possibly connected by a first-order phase transition, indicating that superconducting electrons in TTG may be of spin-triplet nature. (g) Phase diagram of tMBG device with $\theta = 1.08°$ concerning carrier concentration and electric displacement field. The tMBG exhibits significant tunability with strong differences in phase diagrams for $D > 0$ and $D < 0$. (h) Evidence of superconductivity observed from the temperature (T) dependence of resistance (R_{xx}) in TDBG in proximity to WSe_2 for two different samples with twist angles of 1.37° and 1.24°, referred to hereafter as D1 and D2, where ν is the moiré filling factor and D is the displacement field. (i) I–V characteristics of superconductivity as a function of temperature, obtained by integrating $\mathrm{d}V/\mathrm{d}I$ (I_{dc}) at the red marker in (a) (lower inset). $V(I_{dc})$ was used to determine the value of the Berezinskii–Kosterlitz–Thouless transition temperature, $T_{BKT} = 64$ mK (upper inset).

Superconductivity in TBG was first observed by Cao *et al.* in 2018.[6] When the carrier concentration n in TBG is adjusted slightly away from the correlated insulating state ($n = \pm n_s/2$), a superconducting state with a maximum transition temperature of 1.7 K emerges, forming a dome-shaped superconducting phase on each side of the half-filling state, as shown in Fig. 7(b). The critical magnetic field varies significantly with carrier concentration under an applied magnetic field. Moreover, the dependence of the critical magnetic field is consistent with Ginzburg–Landau theory, and oscillatory phenomena due to Josephson junction array structures formed by sample inhomogeneity further confirm the existence of the superconducting state. Similar to the insulating state, subsequent experiments also observed superconducting phases near other integer fillings.[56–59] Compared to other superconductors, two-dimensional heterostructure materials allow for more convenient modulation of electron interaction strength through parameters such as twist angle and pressure,[60,61] and feature clean interlayer interfaces, making carrier concentration adjustment very convenient, thus providing an ideal platform for studying superconducting phenomena.

Although many experiments have observed correlated insulating states and superconductivity in TBG, the origin of superconductivity in TBG and the relationship between the superconducting and correlated insulating phases remain controversial. Some theories suggest that the correlated insulating state in TBG is a prerequisite for the emergence of superconductivity, similar to the doping-induced superconductivity in Mott insulators observed in cuprate superconductors.[62] There are several similarities between superconductivity in TBG and high-temperature superconductors, the most notable one being that superconductivity in TBG appears on both sides of the correlated insulating state as the carrier concentration varies, resembling the phase diagram of cuprate

superconductors.[62,63] Furthermore, due to strong electron interactions, the ratio of the superconducting transition temperature to the Fermi temperature in TBG is high, exceeding the range observed in conventional superconductors.[6] Temperature-dependent resistance measurements on TBG with doping levels near $\pm n_s/2$ reveal the presence of a strange metallic state within this doping range.[64,65] The resistance versus temperature curve can be roughly divided into three parts: at low temperatures, the curve shows superconducting characteristics with a sudden drop in resistance near the superconducting transition temperature; as the temperature increases, the superconducting state gradually transitions to a correlated insulating state, with the curve exhibiting insulating behavior where the resistance decreases with increasing temperature; beyond a certain temperature, the curve shows a strange metallic state, characterized by a linear relationship between resistance and temperature, $\rho(T) \sim AT$ (where A is a constant). This linear relationship between resistance and temperature is also observed in cuprate superconductors.[66] Additionally, STM measurements on TBG reveal that when the flat band is partially filled, the STS peaks associated with the flat band split, forming a pseudogap, and the weight of the two peaks varies with spatial position. This phenomenon indicates that charge is not uniformly distributed in space but forms a stripe charge order, breaking the C_6 symmetry of the moiré lattice.[46,47] Similar phenomena are confirmed by transport measurements under magnetic fields applied in different directions, showing anisotropic responses in longitudinal resistance to in-plane magnetic fields.[67] Such stripe charge orders are also frequently observed in high-temperature superconductors.[68,69]

However, there is substantial evidence supporting that superconductivity in TBG is not high-temperature superconductivity but conventional superconductivity induced by electron–phonon coupling, and it competes with rather than coexists with the correlated insulating state. In transport measurement devices, when the thickness of the hBN layer between TBG and the bottom graphene gate is smaller than the moiré period, the polarized charges in the gate graphene screen the Coulomb interactions on this scale.[58] The formation of the insulating state requires Coulomb interactions to exceed the bandwidth, but the superconducting state is primarily influenced by the density of states at the Fermi level. Therefore, the screening of Coulomb interactions affects the formation of the insulating state but not the superconducting state. Consequently, when the insulating state disappears, the superconducting state persists and occupies the position originally belonging to the insulating state.[58,59] Adding a monolayer WSe_2 insulator between hBN and TBG or using AB-stacked TBG can also generate a superconducting state without forming an insulating state, and the superconducting state can appear at twist angles much smaller than the magic angle.[57,59] The stabilization of superconductivity with reduced Coulomb interaction supports the hypothesis that superconductivity in TBG originates from electron–phonon coupling, as weaker Coulomb repulsion facilitates Cooper pair formation and stabilizes the superconducting order parameter. In contrast, for high-temperature superconductors, the order parameter strengthens with increased Coulomb interactions. Additionally, the strange metallic state with linear temperature-dependent resistance is theorized to be caused by electron–phonon scattering at high temperatures, with the slope related to the electron–phonon coupling strength.[64,70,71] The origin and nature of superconductivity in TBG remain unresolved and require extensive further investigation.

In addition to the TBG system, the development of van der Waals heterostructure fabrication technology and improved control over twist angles have led to the study of various other twisted systems, including twisted double bilayer graphene (TDBG). Unlike TBG, TDBG inherits the electric field tunability of bilayer Bernal-stacked graphene.[72] This allows TDBG to adjust electron interaction strength by changing the relative twist angle and interlayer coupling, as well as by altering the electric field,[51,72–76] as shown in Fig. 7(c). Consequently, TDBG can exhibit flat bands over a wider range of twist angles, unlike TBG, which is limited to around 1.1°. Without an external displacement field, TDBG features a small bandgap between two flat bands and larger gaps above and below them. Increasing the displacement field broadens the gap between the flat bands while reducing and eventually eliminating the gaps above and below the flat bands.[51,72] Similar to TBG, correlated insulating states have been observed at integer fillings in TDBG.[68,73–76] However, STM experiments reveal that the electron wave functions in TDBG are non-localized, unlike TBG, where they localize in specific stacking regions. In TDBG, the density of states split due to strong correlations appears across all stacking regions, suggesting that the insulating state at $\nu = 2$ might arise from non-local exchange interactions.[77] Additionally, spin Zeeman effect observations in TDBG show a g-factor of approximately 2, indicating spin polarization at $\nu = 2$, unlike the valley polarization seen in TBG.[68,73,75] Liu *et al.* also has observed evidence of potential superconductivity in TDBG, however, it might be due to reduced resistivity resulting from carrier scattering suppression during the ferromagnetic transition of the insulating state.[75] In 2023, Su *et al.* reported their observation of superconductivity in TDBG by placing a few-layer WSe_2 flake in direct contact with the TDBG moiré superlattice,[54] as shown in Fig. 7(h). The superconductivity has been observed in TDBG devices with twist angles of 1.37° and 1.24°. They provided further evidence for superconductivity through observation of Berezinskii–Kosterlitz–Thouless transitions and

a phase coherent interference pattern in the TDBG devices with a twist angle of 1.37°, as shown in Fig. 7(i). whereas, by contrast, superconductivity in the one with a twist angle of 1.24° was weaker. Their work also further highlights the importance of WSe_2 in stabilizing some competing order in the rich yet fragile phase diagram of moiré systems.[78] However, the nature of proximity-induced superconductivity in the TDBG/WSe_2 structure remains an open question.[78] Further exploration is needed to study the superconducting state in TDBG.

Twisted trilayer graphene (TTG) exhibits electric field tunability similar to TBG. TTG is composed of three layers of graphene, with two independent twist angles θ_{BM} and θ_{TM} as an ideal system for the precise tuning of the electronic interlayer coupling to maximize the effect of correlated behaviors.[79] For the special case of mirror symmetric stacking, $\theta_{\mathrm{BM}} = \theta_{\mathrm{TM}} = \theta$ (T and B are aligned, and M is twisted relative to these by an angle θ), TTG is predicted to host two sets of flat bands whose band velocity vanishes at a magic angle of $\theta \sim 1.56°$.[80,81] As in magic-angle twisted trilayer graphene (MATTG), its band structure consists of a combination of the Dirac cones from monolayer graphene and the flat bands from TBG,[52,57,59] and their hybridization can be tuned by the displacement field $\boldsymbol{D}$.[52] Due to the presence of independent Dirac cones, TTG does not exhibit strong insulating behavior at any filling when $D = 0$.[57] As shown in Fig. 7(d), similar to TBG, superconductivity is observed in TTG near integer fillings.[52,57,59,82] For spin-singlet superconductors, superconductivity is suppressed at a certain parallel magnetic field strength due to the Zeeman effect, a limit known as the Pauli limit. However, if electrons pair via spin-triplet coupling to form a superconductor, an external magnetic field will not disrupt the Cooper pairs by increasing the energy difference between the two electrons. Thus, spin-triplet superconductors can maintain superconductivity under higher magnetic fields. TTG's superconductivity is not restricted by the Pauli limit and can persist under magnetic fields up to 10 T, with a second superconducting phase observed as the magnetic field increases, possibly connected by a first-order phase transition[52] (Figs. 7(e) and 7(f)). These phenomena suggest that the superconducting electrons in TTG may form spin-triplet pairs. Additionally, it was found that the divergent density of states at the van Hove singularities does not induce or enhance superconducting order in TTG, and superconductivity can be tuned near the Bose–Einstein condensation crossover point,[59] indicating strong coupling characteristics. Therefore, the superconductivity in TTG is unlikely to be consistent with conventional weak electron–phonon coupling. Some researchers have also modulated the electron interaction strength in TTG by introducing bilayer graphene, yielding results consistent with TBG, where superconductivity can exist without the presence of correlated insulating states, indicating a competitive relationship with electron interactions.[82] However, this experimental result has also led to theoretical proposals that superconductivity originates from extended Cooper pairs formed by skyrmion pairs with opposite Chern numbers through antiferromagnetic coupling, for which the presence of insulating states is not necessary.[83] While the origin of superconductivity in TTG remains controversial, increasing research suggests that C_{2z} symmetry plays a crucial role in the presence of superconducting states in twisted systems.[59,83,84]

In addition to the aforementioned high-symmetry twisted systems, twisted monolayer-bilayer graphene (tMBG), which possesses lower crystalline symmetry, has also begun to attract attention. The tMBG consists of a monolayer graphene and a bilayer Bernal-stacked graphene. Due to the different number of layers in the graphene that make up the tMBG heterojunction, tMBG lacks mirror reflection symmetry and the C_{2z} symmetry present in TBG and TTG, resulting in lower crystalline symmetry. This leads to significant differences in the phase diagrams for $D > 0$ and $D < 0$, but it also exhibits high tunability by electric field,[53,85,86] as shown in Fig. 7(g). Overall, two resistance peaks appear at the fully filled flat band ($\nu = \pm 4$), and the displacement field D can open a gap between the flat bands, with the resistivity increasing as the absolute value of D increases. When $D > 0$, the direction of the displacement field points from the monolayer to the bilayer, and its phase diagram is similar to that of TDBG. At $\nu = 2$, interactions split the fourfold degenerate flat conduction bands into spin-polarized flat bands with a Chern number of 0, leading to correlated insulating behavior.[87,88] Additionally, valley polarization occurs at $\nu = 1$ and $\nu = 3$ under a magnetic field, and Chern insulating states with a Chern number of 2 also appear.[85,87,88] Furthermore, at $D > 0$, characteristics of a uniformly distributed flat band density of states in real space, similar to those in TDBG, have been observed.[89] For $D < 0$, the phase diagram of tMBG resembles that of TBG more closely, but due to tMBG's larger bandwidth, only metallic behavior correlated states are observed at integer fillings, which transition to insulating states upon applying a perpendicular magnetic field.[86] Similar to TBG, when $D < 0$, tMBG also exhibits localized flat band electronic states, concentrated in the ABB stacking region.[89] Given that tMBG features not only correlated states but also flat bands with non-zero Chern numbers,[90] it serves as an ideal platform for studying the interplay between correlated states and topological states.

5.2. Topological insulators and symmetry

In addition to the insulating state observed at half-filling as described in Subsection 5.1, many experiments have also detected insulating states at $\nu = 0, \pm 1, \pm 3$.[56–59,67,91] The insulating state at $\nu = 0$ arises due to the breaking of C_2 symme-

try when TBG is aligned with a boron nitride substrate at zero angle, opening a gap at the Dirac point between the conduction and valence bands, thus forming flat Chern bands. Insulating states at other integer fillings which can be stabilized by modest magnetic fields occur because electron interactions can break the C_2T symmetry of the system (time-reversal symmetry is broken by an interaction-induced Haldane mass, which is a strong correlation effect during changing fillings and opens a mass gap of equal and opposite magnitude in the K and K' valleys), resulting in spin and valley polarized flat bands.[91] Consequently, interaction-induced insulating states appear at all integer ν values.[92] The breaking of C_2T symmetry and the emergence of gaps are closely related to the twist angle and interaction strength; even near the magic angle, insulating states only appear within a specific interaction range. Although breaking both C_2 and T symmetries can produce flat Chern bands, breaking C_2 symmetry reverses the sign of the valley Chern number, whereas breaking T symmetry does not, leading to different Chern numbers for the resulting flat bands.[91,93,94]

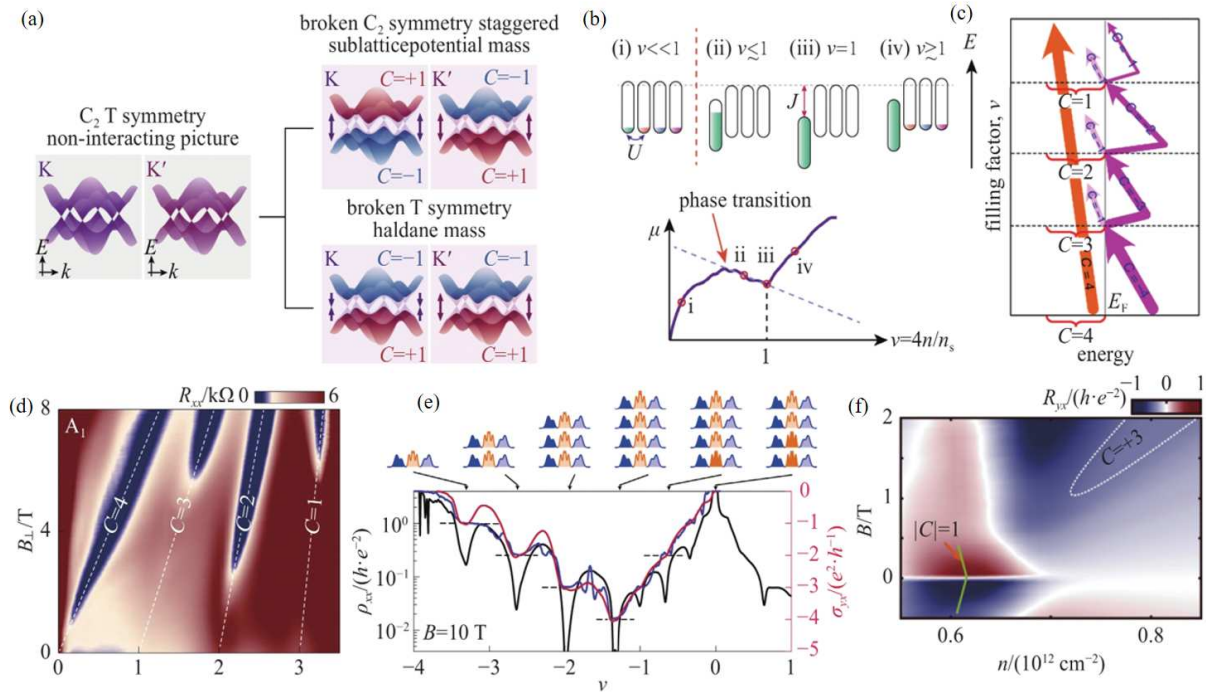


Fig. 8. Chern insulator and time-reversal symmetry in MATBG.[55,91,93,96–98] (a) The Chern numbers associated with each flat band depend on the specific symmetry-breaking mechanism. This panel illustrates how the band Chern numbers in MATBG change when C_{2z} symmetry and time-reversal symmetry are broken. (b) The upper part of the panel depicts the cascade filling sequence in MATBG, while the lower part shows the corresponding relationship between the chemical potential and the filling factor in MATBG. A cascade phase transition occurs before integer fillings, driven by exchange interactions that redistribute carriers into one band while elevating the other three bands to higher energies. (c) A schematic diagram illustrating the evolution of the system's Chern numbers during a cascade phase transition under time-reversal symmetry breaking in MATBG. (d) Color plot of R_{xx} versus ν and $B_\perp$, measured at $T = 1.5$ K, showing experimentally observed Chern insulator states at various filling factors of MATBG. At fillings $\nu = \pm1, \pm2, \pm3, 0$, the corresponding Chern numbers $C = \pm1, \pm2, \pm3, \pm4$ are consistent with the Chern number changes induced by breaking time-reversal symmetry. (e) The variation in longitudinal resistance and Hall conductance with filling of MATBG, showing flat band reconstruction induced by a magnetic field. The upper part of the panel shows the occupied reconstructed bands. (f) Around $\nu = 0.8$, MATBG undergoes a transition from a Chern number with an absolute value of 1 to 3 at a magnetic field of approximately 0.5 T.

Due to the nontrivial topological properties of the flat bands, the insulating states in magic-angle twisted graphene systems exhibit nonzero Chern numbers. For a magic-angle graphene composed of M and N layers, when the upper and lower layers are stacked with the same chirality, the total Chern number for the two flat bands in each valley is $\pm(M-N)$. Conversely, when the upper and lower layers are stacked with opposite chirality, the total Chern number for the two flat bands in each valley is $\pm(M-N-2)$. The significant energy gap between the flat bands and the high-energy bands confers strong stability to the total Chern number of the two flat bands.[95] However, the Chern number for each individual flat band is susceptible to various factors, including the twist angle, Coulomb interaction strength, and external magnetic field intensity.[56] Additionally, the Chern number is influenced by the manner of symmetry breaking. Either aligning graphene with boron nitride to break the C_{2z} symmetry or breaking the time-reversal symmetry can reduce the flat band degeneracy and open a gap between them, resulting in bands with nonzero Chern numbers (Fig. 8(a)). During the doping process, as the carrier concentration increases, theoretically, all four spin and valley bands in the central flat band (CFB) should be uniformly filled. However, before reaching integer filling, a cascade of phase transitions occurs, where exchange

interactions transfer all carriers to one specific band and push the other three bands to higher energies (Fig. 8(b)).[55,96]

For magic-angle twisted bilayer graphene (MATBG), the Chern insulators in the presence of a magnetic field often exhibit broken time-reversal symmetry.[93] Specifically, at fillings $\nu = \pm 1, \pm 2, \pm 3, 0$, the corresponding Chern numbers are $C = \pm 1, \pm 2, \pm 3, \pm 4$, as illustrated in Fig. 8(c), with the experimental results shown in Fig. 8(d). Furthermore, the thermal activation gap Δ in TBG responds differently to an external magnetic field depending on the filling. At $\nu = 2$, Δ decreases with increasing magnetic field, whereas at $\nu = 1, 3$, Δ increases. This indicates that TBG is in a valley-polarized or inter-valley coherent state at $\nu = 2$, and in a spin-polarized state at $\nu = 1,\ 3$.[99] Besides MATBG, other twisted systems also exhibit Chern insulators with nonzero Chern numbers. For instance, based on the relationship between the magnetic field value at which the topological gap closes and the Chern number, a $C = 2$ insulator has been inferred in TDBG with $\theta = 1.01°$.[73] Additionally, by adjusting the displacement field, a Chern insulator with $C = 2$ has been observed in ABC-stacked trilayer graphene at $\nu = -1$.[100]

As a common method to break time-reversal symmetry, a magnetic field can not only induce the formation of Chern insulators but also give rise to Landau levels, leading to the reconstruction of flat bands. For instance, in MATBG as shown in Fig. 8(e), the zeroth Landau level evolves into a Chern band with $C = 2$. To maintain a total Chern number of zero, the flat bands adjacent to the $C = 2$ Chern band have Chern numbers of -1. Therefore, for each spin and valley, the magnetic field reconstructs two flat bands into three sub-bands.[97] Furthermore, under the influence of a magnetic field, there is a competitive relationship between different Chern insulators. In the absence of a magnetic field, the ground state at integer fillings is a many-body degenerate ground state, each with a different Chern number. Ignoring chiral perturbations, the state with the smaller Chern number is favored. However, the presence of a magnetic field lowers the energy of states with larger Chern numbers, enhancing their competitive advantage over states with smaller Chern numbers. Experimentally, this is observed in MATBG near $\nu = 0.8$, where the absolute value of the Chern number transitions from 1 to 3 at a magnetic field of approximately 0.5 T[98] (Fig. 8(f)).

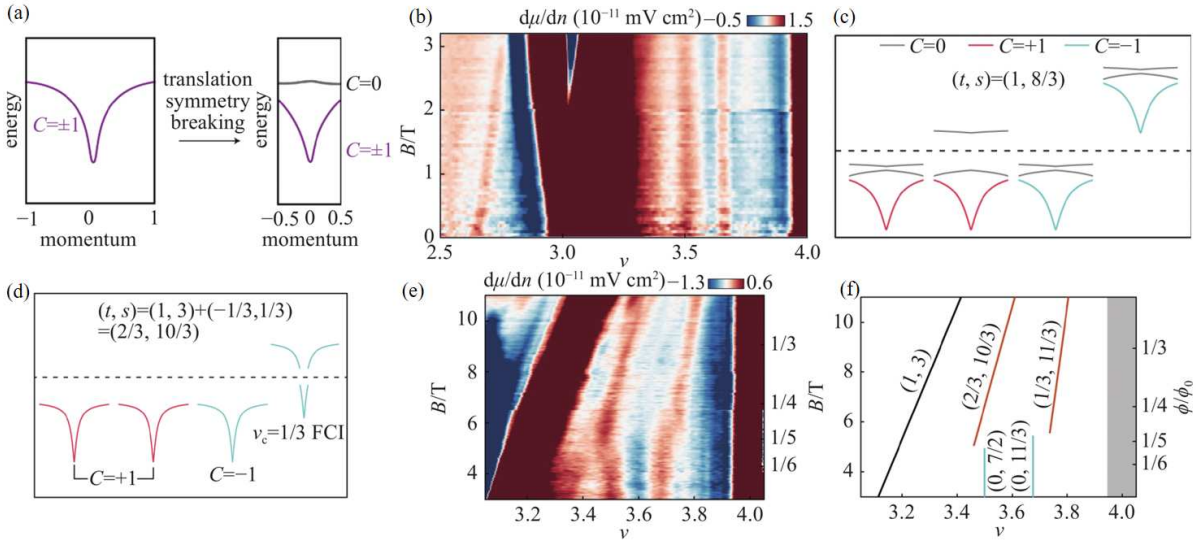


Fig. 9. Chen insulators and spatial symmetry in MATBG.[101–104] (a) Schematic illustration of the Brillouin zone folding due to the breaking of translational symmetry, leading to the emergence of a new band with a Chern number of zero and a doubling of the total number of bands. (b) Local inverse compressibility coefficients between $B = 0$ T and 3 T for fillings $\nu = 2.5$ to 4, showing the presence of a SBCI state with $(t, s) = (1, 8/3)$ at $\nu = 8/3$. (c) Schematic representation of the formation of the SBCI state with $(t, s) = (1, 8/3)$ observed in (b), with a tripling of the Brillouin zone. (d) Local inverse compressibility coefficients between $B = 3$ T and 11 T for fillings $\nu = 3$ and 4, illustrating the presence of different states. (e) Wannier diagrams obtained from measurements in (d), showing the transition from a charge-density wave (CDW) state to a fractional Chern insulator (FCI) state with increasing magnetic field. (f) Schematic depiction of the formation of the FCI state with $(t, s) = (2/3, 10/3)$, which can be considered as a superposition of the previous $(1, 3)$ Chern insulator state and $(-1/3, 1/3)$ FCI state.

Breaking spatial symmetry is crucial for the states of Chern insulators. Beyond the aforementioned C_{2z} symmetry, the modulation of charge density under electron interactions can lead to an uneven energy distribution in the Brillouin zone. This causes translational symmetry breaking and reduces the system's energy by folding the Brillouin zone. In TBG, since the Berry curvature is mainly concentrated at the Γ point, folding the Brillouin zone generates a new band with a zero Chern number, effectively doubling the total number of bands (Fig. 9(a)). This can result in new Chern insulator states at different fillings.[101]

Translational symmetry breaking can also lead to higher-order folding of the Brillouin zone. For example, experiments have observed a symmetry-broken Chern insulator (SBCI) state formed by tripling the Brillouin zone folding, as shown in Figs. 9(b) and 8(c). This theory can also explain the tran-

sition of FCI states. For instance, the $(2/3, 10/3)$ FCI state in Fig. 10(d), with a Chern number and filling factor of 2/3 and 10/3, respectively, can be viewed as a superposition of a $(1,3)$ Chern insulator state and a $(-1/3, 1/3)$ FCI state.[102]

Figures 9(e) and 9(f) illustrate the competition between CDW and FCI states. However, as a magnetic field increases the uniformity of Berry curvature distribution within the Brillouin zone, it makes the folding of the Brillouin zone less likely, thereby favoring the formation of FCI states.[103,104] Consequently, CDW states gradually transition into FCI states with increasing magnetic field strength. Additionally, in TBG on a WSe_2 substrate, an SBCI state with Chern numbers of $(-4, -0.5)$ due to double Brillouin zone folding has been observed.[105] These findings underscore the importance of symmetry breaking.

5.3. Quantum anomalous Hall effects

Quantum anomalous Hall (QAH) effect means a state with a quantized Hall conductance can exist without an external magnetic field at all. Theoretically, the first explicit model with quantized Hall conductance in the absence of magnetic fields was constructed by Haldane[106] in the honeycomb lattice. In 2005, Qi *et al.*[107] discussed the possibility of the QAH effect in semiconductors, and proposed a different two-band, tight-binding model with the QAH phase, which is defined on the square lattice and has low energy excitations around momentum $\boldsymbol{k} = \boldsymbol{0}$. Based on the model, there are two conditions that will guide our search for realistic quantum anomalous Hall materials: (a) inverted band structures and (b) ferromagnetic insulators.[108] The theoretical prediction was verified by experiments soon afterward. In 2013, Chang *et al.* had an experimental observation of the quantum anomalous Hall effect in the thin films of the compound $Cr_{0.15}(Bi_{0.1}Sb_{0.9})_{1.85}Te_3$, with Cr as the magnetic dopant.[109]

In moiré materials, Serlin *et al.* reported the observation of a QAH effect in twisted bilayer graphene aligned to hexagonal boron nitride.[110] In a flat-band ($\theta \approx 1.15^\circ \pm 0.01^\circ$) TBG sample aligned to hBN, R_{xy} approached h/e^2 in a narrow range of density near $\nu = 3$ ($n = 2.37 \times 10^{12}$ cm^{-2}), concomitant with a deep minimum in R_{xx} (Figs. 10(a) and 10(b)). Tseng *et al.* also reported QAH at half filling in TBG.[113] Geisenhof *et al.* reported QAH octet driven by orbital magnetism in bilayer graphene.[114]

Contrary to theoretical predictions, the recent studies by Shan and Mak's groups[111] unexpectedly observed the quantum anomalous Hall effect (QAHE) and a possible quantum spin Hall effect (QSHE) in the valence band of an AB-stacked $MoTe_2/WSe_2$ moiré heterostructure. As previously mentioned, the key to realizing topological bands in moiré heterostructures theoretically lies in the presence of two nearly degenerate bands, making the moiré superlattice structure effectively equivalent to a hexagonal lattice. In the $MoTe_2/WSe_2$ heterostructure, the band offset in the valence band is approximately 200 meV.[115] This offset can be reduced by an external electric field, bringing the two bands closer to degeneracy. The electric field effectively tunes the strength of interlayer hopping, i.e., the weight of the hole wavefunction in the two layers, thereby enabling band inversion and a topological phase transition between the moiré subbands. Experimentally, at filling factor $\nu = 1$, a field-induced phase transition from a Mott insulator to a quantum anomalous Hall state was observed, accompanied by a clear quantized Hall conductance in the QAHE regime (Fig. 10(d)). The highest temperature at which quantization was achieved was approximately 2 K, which is relatively high compared to other known QAHE systems.[85,109,110,116,117] Notably, unlike conventional topological phase transitions, yet no bandgap closing was observed during the transition from a Mott insulator to a QAHE in which Chern number is changing from 0 in the Mott insulator to -1 in the QAHE state. This absence of gap closing could be due to a sudden change in spin order symmetry before and after the phase transition.

Moreover, the fractional quantum anomalous Hall effect (FQAHE) has been observed in moiré superlattice materials. The FQAHE is characterized by the emergence of exotic electron fluids with fractionally charged excitations, resulting from strong electron–electron interactions in partially filled topological bands, all in the absence of an external magnetic field. Theoretically, this phenomenon is predicted to occur in topologically nontrivial flat bands when spontaneous time-reversal symmetry breaking takes place. The realization of topological flat bands in moiré superlattices presents a promising avenue for achieving lattice analogs of the fractional quantum Hall effect without requiring an external magnetic field. In 2023, Cai *et al.* reported signatures of FQAH states in twisted $MoTe_2$ in AA-stacked $MoTe_2$ bilayer devices with twist angle about 3.7°.[118] They obtained a Landau fan diagram showing linear shifts in carrier densities corresponding to filling factor $\nu = -2/3$ and $\nu = -3/5$ ferromagnetic states with applied magnetic field. These shifts match the Streda formula dispersion of FQAH states with fractionally quantized Hall conductance of $\sigma_{xy} = \frac{2e^2}{3h}$ and $\sigma_{xy} = \frac{3e^2}{5h}$, respectively. Xu *et al.* also observed well-quantized Hall resistance of h/e^2 around moiré filling factor $\nu = -2/3$, and nearly quantized Hall resistance of $3h/(2e^2)$ around $\nu = -2/3$, respectively, in twisted $MoTe_2$.[119] In pentalayer graphene-hBN moiré superlattice, Lu *et al.* observed plateaus of quantized Hall resistance $R_{xy} = \frac{\nu}{he^2}$ at $\nu > 1$, 2/3, 3/5, 4/7, 4/9, 3/7 and 2/5 of the moiré superlattice respectively at zero magnetic field, breaking the limit of $\nu > 1/2$ in $MoTe_2$[112] (Fig. 10(e)).

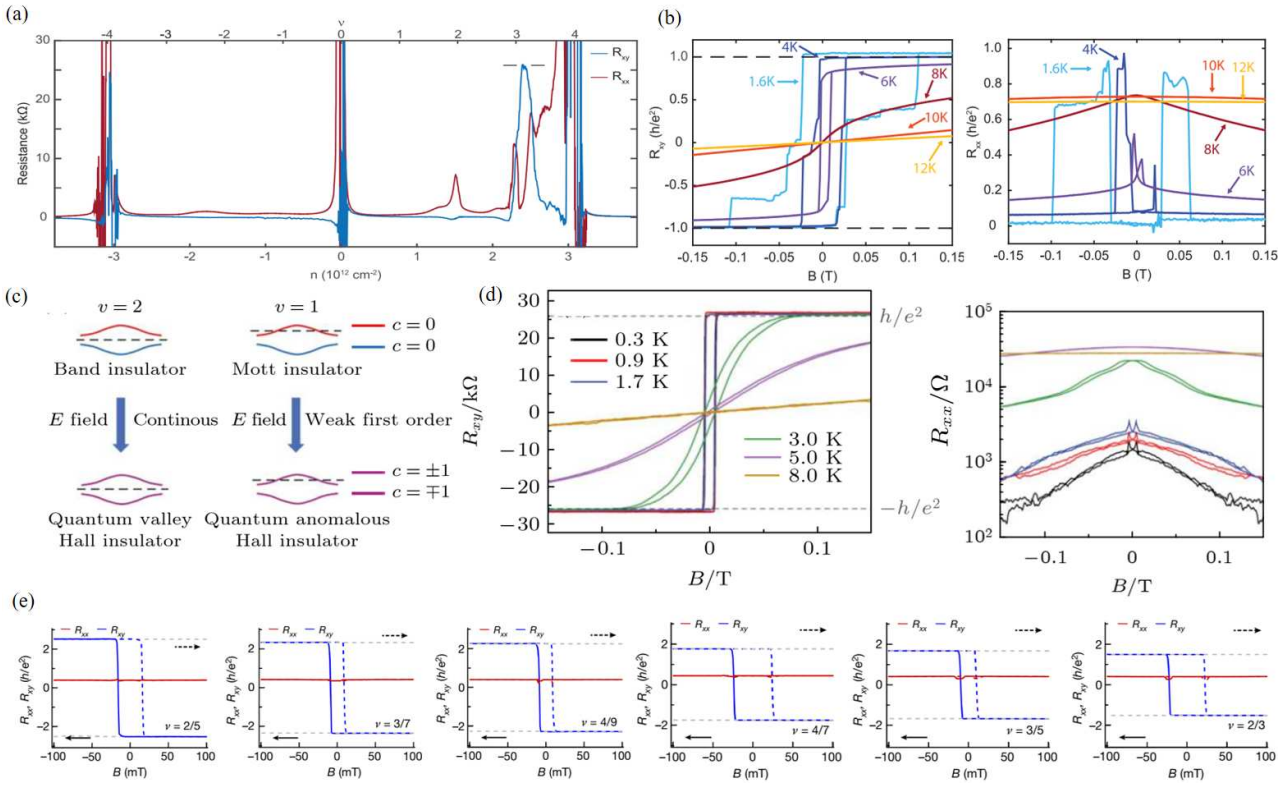


Fig. 10. Quantum anomalous Hall effects.[110–112] (a) and (b) QAH effect in TBG ($\theta \approx 1.15^\circ \pm 0.01^\circ$). (a) R_{xy} approaching h/e^2 in a narrow range of density near $\nu = 3$ ($n = 2.37 \times 10^{12}$ cm^{-2}), concomitant with a deep minimum in R_{xx}, measured at a magnetic field $B = 150$ mT and temperature $T = 1.6$ K. (b) R_{xy} and R_{xx} as a function of B measured at various temperatures for $n = 2.37 \times 10^{12}$ cm^{-2}. (c) and (d) Topological states in AB-stacked $WSe_2/MoTe_2$ moiré superlattices. (c) Schematic illustrations of electric field induced topological phase transitions. A band insulator to a quantum spin Hall insulator transition is possible when the first moiré mini band is full-filled, and a Mott insulator to a quantum anomalous Hall insulator transition could occur when the first moiré mini band is half-filled. (d) At the quantum anomalous Hall region, the measured R_{xx} and R_{xy} versus B field at various temperatures are shown respectively. (e) FQAH effect in pentalayer graphene-hBN moiré superlattice, with the twist angle of 0.744°. Magnetic hysteresis scans of R_{xy} and R_{xx} at $\nu = 2/5$, 3/7, 4/9, 4/7, 3/5 and 2/3, showing quantized values of $R_{xy} = \frac{h}{\nu e^2}$ and much smaller R_{xx}.

6. Summary and outlook

Moiré superlattices in two-dimensional quantum materials exhibit a wealth of physical phenomena and can be tuned through various means such as twist angle, pressure, vertical displacement field, and magnetic field. This makes them ideal structures for studying various novel physical properties. This paper primarily explores the diverse and novel physical properties resulting from superlattice structures. It begins by examining the changes in lattice spatial structure and band structure induced by superlattices, including topics such as secondary Dirac points, van Hove singularities, and atomic reconstruction. Next, it focuses on phenomena related to strong electron correlations in superlattice structures with flat bands, including correlated insulating states, superconductivity, Chern insulators, and symmetry-related properties. Additionally, superlattice structures provide an ideal platform for studying the interplay between various physical phenomena. For example, the superconducting phenomena observed in TBG and TTG might pave new paths for exploring unconventional superconductivity, despite the origins of these states and correlated insulators remaining debated. Furthermore, superlattice structures with both topologically nontrivial flat bands and strong electron interactions are excellent systems for exploring the interplay between topology and strong correlation effects.

Acknowledgments

Project supported by the National Key R&D Program of China (Grant No. 2019YFA0307800), the National Natural Science Foundation of China (Grant No. 12074377), Fundamental Research Funds for the Central Universities, the International Partnership Program of Chinese Academy of Sciences (Grant No. 211211KYSB20210007), the China Postdoctoral Science Foundation (Grant No. 2024M753465), the Postdoctoral Fellowship Program (Grade C) of China Postdoctoral Science Foundation (Grant No. GZC20241893).

References

[1] Hunt B, Sanchez-Yamagishi J D, Young A F, Yankowitz M, LeRoy B J, Watanabe K, Taniguchi T, Moon P, Koshino M, Jarillo-Herrero P and Ashoori R C 2013 *Science* **340** 1427

[2] Dean C R, Wang L, Maher P, Forsythe C, Ghahari F, Gao Y, Katoch J, Ishigami M, Moon P, Koshino M, *et al.* 2013 *Nature* **497** 598

[3] Ponomarenko L, Gorbachev R, Yu G, Elias D, Jalil R, Patel A, Mishchenko A, Mayorov A, Woods C, Wallbank J, *et al.* 2013 *Nature* **497** 594

[4] Yankowitz M, Xue J, Cormode D, Sanchez-Yamagishi J D, Watanabe K, Taniguchi T, Jarillo-Herrero P, Jacquod P and LeRoy B J 2012 *Nat. Phys.* **8** 382

[5] Yang W, Chen G, Shi Z, Liu C C, Zhang L, Xie G, Cheng M, Wang D, Yang R, Shi D, *et al.* 2013 *Nat. Mater.* **12** 792

[6] Cao Y, Fatemi V, Fang S, Watanabe K, Taniguchi T, Kaxiras E and Jarillo-Herrero P 2018 *Nature* **556** 43

[7] Cao Y, Fatemi V, Demir A, Fang S, Tomarken S L, Luo J Y, Sanchez-Yamagishi J D, Watanabe K, Taniguchi T, Kaxiras E, *et al.* 2018 *Nature* **556** 80

[8] Schmidt H, Luedtke T, Barthold P, Mccann E, Fal'Ko V I and Haug R J 2008 *Appl. Phys. Lett.* **93** 666

[9] Wang H, Ma S, Zhang S and Lei D 2022 *Light: Sci. Appl.* **11** 159

[10] Brihuega I, Mallet P, González-Herrero H, Trambly de Laissardière G, Ugeda M M, Magaud L, Gómez-Rodríguez J M, Ynduráin F and Veuillen J Y 2012 *Phys. Rev. Lett.* **109** 196802

[11] Lopes dos Santos J M B, Peres N M R and Castro Neto A H 2007 *Phys. Rev. Lett.* **99** 256802

[12] Gorbachev R V, Riaz I, Nair R R, Jalil R, Britnell L, Belle B D, Hill E W, Novoselov K S, Watanabe K and Taniguchi T 2011 *Small* **7** 465

[13] Woods C, Britnell L, Eckmann A, Ma R, Lu J, Guo H, Lin X, Yu G, Cao Y, Gorbachev R V, *et al.* 2014 *Nat. Phys.* **10** 451

[14] Woods C, Withers F, Zhu M, Cao Y, Yu G, Kozikov A, Ben Shalom M, Morozov S, Van Wijk M, Fasolino A, *et al.* 2016 *Nat. Commun.* **7** 10800

[15] Yoo H, Engelke R, Carr S, Fang S, Zhang K, Cazeaux P, Sung S H, Hovden R, Tsen A W, Taniguchi T, *et al.* 2019 *Nat. Mater.* **18** 448

[16] Yankowitz M, Watanabe K, Taniguchi T, San-Jose P and LeRoy B J 2016 *Nat. Commun.* **7** 13168

[17] Rosenberger M R, Chuang H J, Phillips M, Oleshko V P, McCreary K M, Sivaram S V, Hellberg C S and Jonker B T 2020 *ACS Nano* **14** 4550

[18] Butz B, Dolle C, Niekiel F, Weber K, Waldmann D, Weber H B, Meyer B and Spiecker E 2014 *Nature* **505** 533

[19] Lin J, Fang W, Zhou W, Lupini A R, Idrobo J C, Kong J, Pennycook S J and Pantelides S T 2013 *Nano Lett.* **13** 3262

[20] Van Hove L 1953 *Phys. Rev.* **89** 1189

[21] He W Y, Su Y, Yang M and He L 2014 *Phys. Rev. B* **89** 125418

[22] He W Y, Chu Z D and He L 2013 *Phys. Rev. Lett.* **111** 066803

[23] Li G, Luican A, Lopes dos Santos J, Castro Neto A, Reina A, Kong J and Andrei E 2010 *Nat. Phys.* **6** 109

[24] Cherkez V, de Laissardi'ere G T, Mallet P and Veuillen J Y 2015 *Phys. Rev. B* **91** 155428

[25] Luican A, Li G, Reina A, Kong J, Nair R R, Novoselov K S, Geim A K and Andrei E Y 2011 *Phys. Rev. Lett.* **106** 126802

[26] Miller D L, Kubista K D, Rutter G M, Ruan M, de Heer W A, First P N and Stroscio J A 2009 *Science* **324** 924

[27] Yin L J, Qiao J B, Wang W X, Zuo W J, Yan W, Xu R, Dou R F, Nie J C and He L 2015 *Phys. Rev. B* **92** 201408

[28] Wong D, Wang Y, Jung J, Pezzini S, DaSilva A M, Tsai H Z, Jung H S, Khajeh R, Kim Y, Lee J, Kahn S, Tollabimazraehno S, Rasool H, Watanabe K, Taniguchi T, Zettl A, Adam S, MacDonald A H and Crommie M F 2015 *Phys. Rev. B* **92** 155409

[29] Yan W, Meng L, Liu M, Qiao J B, Chu Z D, Dou R F, Liu Z, Nie J C, Naugle D G and He L 2014 *Phys. Rev. B* **90** 115402

[30] Laissardi'ere G T D, Mayou D and Magaud L 2010 *Nano Lett.* **10** 804

[31] Yan W, Liu M, Dou R F, Meng L, Feng L, Chu Z D, Zhang Y, Liu Z, Nie J C and He L 2012 *Phys. Rev. Lett.* **109** 126801

[32] Nandkishore R, Levitov L S and Chubukov A V 2012 *Nat. Phys.* **8** 158

[33] Kim K, Coh S, Tan L Z, Regan W, Yuk J M, Chatterjee E, Crommie M F, Cohen M L, Louie S G and Zettl A 2012 *Phys. Rev. Lett.* **108** 246103

[34] Yuan N F, Isobe H and Fu L 2019 *Nat. Commun.* **10** 5769

[35] Park C H, Yang L, Son Y W, Cohen M L and Louie S G 2008 *Phys. Rev. Lett.* **101** 126804

[36] Wolf T M R, Zilberberg O, Levkivskyi I and Blatter G 2018 *Phys. Rev. B* **98** 125408

[37] Ortix C, Yang L and van den Brink J 2012 *Phys. Rev. B* **86** 081405

[38] Park C H, Yang L, Son Y W, Cohen M L and Louie S G 2008 *Nat. Phys.* **4** 213

[39] Wallbank J R, Patel A A, Mucha-Kruczyński M, Geim A K and Fal'ko V I 2013 *Phys. Rev. B* **87** 245408

[40] Wang E, Lu X, Ding S, Yao W, Yan M, Wan G, Deng K, Wang S, Chen G, Ma L, *et al.* 2016 *Nat. Phys.* **12** 1111

[41] Yan H, Chu Z D, Yan W, Liu M, Meng L, Yang M, Fan Y, Wang J, Dou R F, Zhang Y, Liu Z, Nie J C and He L 2013 *Phys. Rev. B* **87** 075405

[42] Checkelsky J G, Bernevig B A, Coleman P, Si Q and Paschen S 2024 *Nat. Rev. Mater.* **9** 509

[43] Bistritzer R and MacDonald A H 2011 *Proc. Nat. Acad. Sci. USA* **108** 12233

[44] Wu F, Lovorn T, Tutuc E and MacDonald A H 2018 *Phys. Rev. Lett.* **121** 026402

[45] Choi Y, Kemmer J, Peng Y, Thomson A, Arora H, Polski R, Zhang Y, Ren H, Alicea J, Refael G, *et al.* 2019 *Nat. Phys.* **15** 1174

[46] Jiang Y, Lai X, Watanabe K, Taniguchi T, Haule K, Mao J and Andrei E Y 2019 *Nature* **573** 91

[47] Kerelsky A, McGilly L J, Kennes D M, Xian L, Yankowitz M, Chen S, Watanabe K, Taniguchi T, Hone J, Dean C, *et al.* 2019 *Nature* **572** 95

[48] Xie Y, Lian B, Jäck B, Liu X, Chiu C L, Watanabe K, Taniguchi T, Bernevig B A and Yazdani A 2019 *Nature* **572** 101

[49] Kim K, DaSilva A, Huang S, Fallahazad B, Larentis S, Taniguchi T, Watanabe K, LeRoy B J, MacDonald A H and Tutuc E 2017 *Proc. Nat. Acad. Sci. USA* **114** 3364

[50] Mott N 1990 *J. Solid State Chem.* **88** 5

[51] Cao Y, Rodan-Legrain D, Rubies-Bigorda O, Park J M, Watanabe K, Taniguchi T and Jarillo-Herrero P 2020 *Nature* **583** 215

[52] Cao Y, Park J M, Watanabe K, Taniguchi T and Jarillo-Herrero P 2021 *Nature* **595** 526

[53] Chen S, He M, Zhang Y H, Hsieh V, Fei Z, Watanabe K, Taniguchi T, Cobden D H, Xu X, Dean C R, *et al.* 2021 *Nat. Phys.* **17** 374

[54] Su R, Kuiri M, Watanabe K, Taniguchi T and Folk J 2023 *Nat. Mater.* **22** 1332

[55] Park J M, Cao Y, Watanabe K, Taniguchi T and Jarillo-Herrero P 2021 *Nature* **592** 43

[56] Lu X, Stepanov P, Yang W, Xie M, Aamir M A, Das I, Urgell C, Watanabe K, Taniguchi T, Zhang G, *et al.* 2019 *Nature* **574** 653

[57] Arora H S, Polski R, Zhang Y, Thomson A, Choi Y, Kim H, Lin Z, Wilson I Z, Xu X, Chu J H, *et al.* 2020 *Nature* **583** 379

[58] Saito Y, Ge J, Watanabe K, Taniguchi T and Young A F 2020 *Nat. Phys.* **16** 926

[59] Stepanov P, Das I, Lu X, Fahimniya A, Watanabe K, Taniguchi T, Koppens F H, Lischner J, Levitov L and Efetov D K 2020 *Nature* **583** 375

[60] Finney N R, Yankowitz M, Muraleetharan L, Watanabe K, Taniguchi T, Dean C R and Hone J 2019 *Nat. Nanotechnol.* **14** 1029

[61] Yankowitz M, Chen S, Polshyn H, Zhang Y, Watanabe K, Taniguchi T, Graf D, Young A F and Dean C R 2019 *Science* **363** 1059

[62] Lee P A, Nagaosa N and Wen X G 2006 *Rev. Mod. Phys.* **78** 17

[63] Keimer B, Kivelson S A, Norman M R, Uchida S and Zaanen J 2015 *Nature* **518** 179

[64] Polshyn H, Yankowitz M, Chen S, Zhang Y, Watanabe K, Taniguchi T, Dean C R and Young A F 2019 *Nat. Phys.* **15** 1011

[65] Codecido E, Wang Q, Koester R, Che S, Tian H, Lv R, Tran S, Watanabe K, Taniguchi T, Zhang F, *et al.* 2019 *Sci. Adv.* **5** eaaw9770

[66] Bruin J A N, Sakai H, Perry R S and Mackenzie A 2013 *Science* **339** 804

[67] Cao Y, Rodan-Legrain D, Park J M, Yuan N F, Watanabe K, Taniguchi T, Fernandes R M, Fu L and Jarillo-Herrero P 2021 *Science* **372** 264

[68] Comin R, Sutarto R, He F, da Silva Neto E, Chauviere L, Frano A, Liang R, Hardy W, Bonn D, Yoshida Y, *et al.* 2015 *Nat. Mater.* **14** 796

[69] Mukhopadhyay S, Sharma R, Kim C K, Edkins S D, Hamidian M H, Eisaki H, Uchida S i, Kim E A, Lawler M J, Mackenzie A P, *et al.* 2019 *Proc. Nat. Acad. Sci. USA* **116** 13249

[70] Wu F, Hwang E and Das Sarma S 2019 *Phys. Rev. B* **99** 165112

[71] Sharma G, Yudhistira I, Chakraborty N, Ho D Y, Ezzi M A, Fuhrer M S, Vignale G and Adam S 2021 *Nat. Commun.* **12** 5737

[72] Adak P C, Sinha S, Ghorai U, Sangani L D V, Watanabe K, Taniguchi T, Sensarma R and Deshmukh M M 2020 *Phys. Rev. B* **101** 125428

[73] Burg G W, Zhu J, Taniguchi T, Watanabe K, MacDonald A H and Tutuc E 2019 *Phys. Rev. Lett.* **123** 197702

[74] He M, Li Y, Cai J, Liu Y, Watanabe K, Taniguchi T, Xu X and Yankowitz M 2021 *Nat. Phys.* **17** 26

[75] Liu X, Hao Z, Khalaf E, Lee J Y, Ronen Y, Yoo H, Haei Najafabadi D, Watanabe K, Taniguchi T, Vishwanath A, *et al.* 2020 *Nature* **583** 221

[76] Shen C, Chu Y, Wu Q, Li N, Wang S, Zhao Y, Tang J, Liu J, Tian J, Watanabe K, *et al.* 2020 *Nat. Phys.* **16** 520

[77] Zhang C, Zhu T, Kahn S, Li S, Yang B, Herbig C, Wu X, Li H, Watanabe K, Taniguchi T, *et al.* 2021 *Nat. Commun.* **12** 2516

[78] Yang W and Zhang G 2023 *Nat. Mater.* **22** 1285
[79] Zhu Z, Carr S, Massatt D, Luskin M and Kaxiras E 2020 *Phys. Rev. Lett.* **125** 116404
[80] Khalaf E, Kruchkov A J, Tarnopolsky G and Vishwanath A 2019 *Phys. Rev. B* **100** 085109
[81] Li X, Wu F and MacDonald A H 2019 *Electronic Structure of Single-twist Trilayer Graphene*
[82] Liu X, Zhang N J, Watanabe K, Taniguchi T and Li J 2022 *Nat. Phys.* **18** 522
[83] Khalaf E, Chatterjee S, Bultinck N, Zaletel M P and Vishwanath A 2021 *Sci. Adv.* **7** eabf5299
[84] Fischer A, Goodwin Z A, Mostofi A A, Lischner J, Kennes D M and Klebl L 2022 *npj Quantum Mater.* **7** 5
[85] Polshyn H, Zhu J, Kumar M A, Zhang Y, Yang F, Tschirhart C L, Serlin M, Watanabe K, Taniguchi T, MacDonald A H, *et al.* 2020 *Nature* **588** 66
[86] Xu S, Al Ezzi M M, Balakrishnan N, Garcia-Ruiz A, Tsim B, Mullan C, Barrier J, Xin N, Piot B A, Taniguchi T, *et al.* 2021 *Nat. Phys.* **17** 619
[87] Polshyn H, Zhang Y, Kumar M A, Soejima T, Ledwith P, Watanabe K, Taniguchi T, Vishwanath A, Zaletel M P and Young A F 2022 *Nat. Phys.* **18** 42
[88] He M, Zhang Y H, Li Y, Fei Z, Watanabe K, Taniguchi T, Xu X and Yankowitz M 2021 *Nat. Commun.* **12** 4727
[89] Tong L H, Tong Q, Yang L Z, Zhou Y Y, Wu Q, Tian Y, Zhang L, Zhang L, Qin Z and Yin L J 2022 *Phys. Rev. Lett.* **128** 126401
[90] Li S Y, Wang Z, Xue Y, Wang Y, Zhang S, Liu J, Zhu Z, Watanabe K, Taniguchi T, Gao H J, *et al.* 2022 *Nat. Commun.* **13** 4225
[91] Nuckolls K P, Oh M, Wong D, Lian B, Watanabe K, Taniguchi T, Bernevig B A and Yazdani A 2020 *Nature* **588** 610
[92] Xie M and MacDonald A H 2020 *Phys. Rev. Lett.* **124** 097601
[93] Das I, Lu X, Herzog-Arbeitman J, Song Z D, Watanabe K, Taniguchi T, Bernevig B A and Efetov D K 2021 *Nat. Phys.* **17** 710
[94] Shen C, Ying J, Liu L, Liu J, Li N, Wang S, Tang J, Zhao Y, Chu Y, Watanabe K, *et al.* 2021 *Chin. Phys. Lett.* **38** 047301
[95] Liu J, Ma Z, Gao J and Dai X 2019 *Phys. Rev. X* **9** 031021
[96] Choi Y, Kim H, Peng Y, Thomson A, Lewandowski C, Polski R, Zhang Y, Arora H S, Watanabe K, Taniguchi T, *et al.* 2021 *Nature* **589** 536
[97] Saito Y, Ge J, Rademaker L, Watanabe K, Taniguchi T, Abanin D A and Young A F 2021 *Nat. Phys.* **17** 478
[98] Stepanov P, Xie M, Taniguchi T, Watanabe K, Lu X, MacDonald A H, Bernevig B A and Efetov D K 2021 *Phys. Rev. Lett.* **127** 197701
[99] Wu S, Zhang Z, Watanabe K, Taniguchi T and Andrei E Y 2021 *Nat. Mater.* **20** 488
[100] Chen G, Sharpe A L, Fox E J, Zhang Y H, Wang S, Jiang L, Lyu B, Li H, Watanabe K, Taniguchi T, *et al.* 2020 *Nature* **579** 56
[101] Pierce A T, Xie Y, Park J M, Khalaf E, Lee S H, Cao Y, Parker D E, Forrester P R, Chen S, Watanabe K, *et al.* 2021 *Nat. Phys.* **17** 1210
[102] Xie Y, Pierce A T, Park J M, Parker D E, Khalaf E, Ledwith P, Cao Y, Lee S H, Chen S, Forrester P R, *et al.* 2021 *Nature* **600** 439
[103] Ledwith P J, Tarnopolsky G, Khalaf E and Vishwanath A 2020 *Phys. Rev. Res.* **2** 023237
[104] Abouelkomsan A, Liu Z and Bergholtz E J 2020 *Phys. Rev. Lett.* **124** 106803
[105] Bhowmik S, Ghawri B, Leconte N, Appalakondaiah S, Pandey M, Mahapatra P S, Lee D, Watanabe K, Taniguchi T, Jung J, *et al.* 2022 *Nat. Phys.* **18** 639
[106] Haldane F D M 1988 *Phys. Rev. Lett.* **61** 2015
[107] Qi X L, Wu Y S and Zhang S C 2006 *Phys. Rev. B* **74** 085308
[108] Liu C X, Zhang S C and Qi X L 2016 *Ann. Rev. Condens. Matter Phys.* **7** 301
[109] Chang C Z, Zhang J, Feng X, Shen J, Zhang Z, Guo M, Li K, Ou Y, Wei P, Wang L L, Ji Z Q, Feng Y, Ji S, Chen X, Jia J, Dai X, Fang Z, Zhang S C, He K, Wang Y, Lu L, Ma X C and Xue Q K 2013 *Science* **340** 167
[110] Serlin M, Tschirhart C L, Polshyn H, Zhang Y, Zhu J, Watanabe K, Taniguchi T, Balents L and Young A F 2020 *Science* **367** 900
[111] Li T, Jiang S, Shen B, Zhang Y, Li L, Tao Z, Devakul T, Watanabe K, Taniguchi T, Fu L, *et al.* 2021 *Nature* **600** 641
[112] Lu Z, Han T, Yao Y, Reddy A P, Yang J, Seo J, Watanabe K, Taniguchi T, Fu L and Ju L 2024 *Nature* **626** 759
[113] Tseng C C, Ma X, Liu Z, Watanabe K, Taniguchi T, Chu J H and Yankowitz M 2022 *Nat. Phys.* **18** 1038
[114] Geisenhof F R, Winterer F, Seiler A M, Lenz J, Xu T, Zhang F and Weitz R T 2021 *Nature* **598** 53
[115] Liu Y, Stradins P and Wei S H 2016 *Sci. Adv.* **2** e1600069
[116] Deng Y, Yu Y, Shi M Z, Guo Z, Xu Z, Wang J, Chen X H and Zhang Y 2020 *Science* **367** 895
[117] Chang C Z, Zhang J, Feng X, Shen J, Zhang Z, Guo M, Li K, Ou Y, Wei P, Wang L L, *et al.* 2013 *Science* **340** 167
[118] Cai J, Anderson E, Wang C, Zhang X, Liu X, Holtzmann W, Zhang Y, Fan F, Taniguchi T, Watanabe K, *et al.* 2023 *Nature* **622** 63
[119] Xu F, Sun Z, Jia T, Liu C, Xu C, Li C, Gu Y, Watanabe K, Taniguchi T, Tong B, *et al.* 2023 *Phys. Rev. X* **13** 031037